Essential Role for Pro^{21} in Phospholamban for Optimal Inhibition of the Ca-ATPase†

Jinhui Li, Curt B. Boschek, Yijia Xiong, Colette A. Sacksteder, Thomas C. Squier, and Diana J. Bigelow*

Cell Biology and Biochemistry Group, Biological Sciences Division, Pacific Northwest National Laboratory, Richland, Washington 99352

Received June 6, 2005; Revised Manuscript Received September 2, 2005

ABSTRACT: We have investigated the functional role of the flexible hinge region centered near the sequence $TIEMP^{21}$, which connects the N-terminal cytosolic and C-terminal membrane-spanning helical domains of phospholamban (PLB). Specifically, we ask if the conformation of this region is important to attain optimal inhibitory interactions with the Ca-ATPase. A genetically engineered PLB mutant was constructed in which Pro^{21} was mutated to an alanine (P21A-PLB_C); in this construct, all three transmembrane cysteines were substituted with alanines to stabilize the monomeric form of PLB, and a unique cysteine was introduced at position 24 near the hinge element (A24C), permitting the site-specific attachment of fluorescein-5-maleimide (FMal) to monitor structure changes. In agreement with prior measurements in cardiac SR microsomes, the calcium concentration associated with half-maximal activation ($Ca_{1/2}$) of the Ca-ATPase, 290 ± 10 nM, is shifted to 580 ± 20 nM when co-reconstituted with PLB_C (Pro21) as a result of a reduction in the cooperativity associated with the calcium-dependent structural transition. Kinetic simulations indicate that PLB_C association with the Ca-ATPase results in a 75% reduction in the equilibrium constant associated with the formation of the second high-affinity calcium binding site. In comparison, there is a 43% reduction in $KCa_{1/2}$ upon reconstitution of the Ca-ATPase with P21A-PLB_C, which can be simulated by decreasing the equilibrium constant associated with the calcium-dependent structural activation by 50%. The diminished inhibitory action of P21A-PLB_C is associated with alterations in the structure of the hinge element, as evidenced by the diminished solvent accessibility of FMal relative to the native structure. Likewise, increases in the α-helical content and decreases in the mobility of the carboxyl-terminal domain of P21A-PLB_C are observed using circular dichroism and fluorescence spectroscopy. Collectively, these results indicate that the overall dimensions of the carboxyl-terminal domain of PLB are increased through a stabilization of secondary structural elements upon mutation in P21A-PLB_C that result in a reduction in the ability of the amino-terminal cytosolic portion of PLB to productively inhibit the Ca-ATPase. Further, these results suggest that the unstructured characteristics of the flexible hinge region in PLB are critical for optimal inhibitory interactions with the Ca-ATPase and suggest its role as a conformational switch.

Phospholamban (PLB),[1] a 52 amino acid integral membrane protein, constitutes a key element in the responsiveness of muscle contractility to β-adrenergic stimulation through its regulation of the sarcoplasmic reticulum (SR) Ca-ATPase (*1*). The SR Ca-ATPase mediates muscle relaxation by the active transport of cytosolic calcium ions into the SR lumen after each contractile event, which is induced by rapid release of calcium into the cytosol through ryanodine receptor calcium channels (*2*). As the limiting step in contractility, the resequestration of cytosolic calcium provides a major control point for both contractile function and calcium signaling events within the cell (*3*).

PLB is coexpressed with the SERCA2a isoform of the Ca-ATPase in cardiac, smooth, and slow-twitch skeletal muscle, where the nonphosphorylated form of PLB inhibits the Ca-ATPase. Upon phosphorylation of PLB at Ser^{16} or Thr^{17}, mediated in vivo by PKA or CaM-kinase II, respectively, this inhibition is relieved, with concomitant increases in rates of calcium transport. PLB regulation of Ca-ATPase activity is manifested by alteration in the calcium concentration dependence of Ca-ATPase activity; phosphorylation of PLB results in a shift in the calcium concentration associated with half-maximal activity ($Ca_{1/2}$) toward lower free calcium concentrations. From equilibrium calcium binding measurements, it has been demonstrated that this calcium shift reflects a reduction in cooperativity between high-affinity calcium binding sites of the Ca-ATPase in the presence of PLB,

† This work was supported by a grant from the National Institutes of Health (HL64031).

* Corresponding author: Cell Biology & Biochemistry Group, Pacific Northwest National Laboratory, P.O. Box 999, MS P7-56, Richland, WA 99352. Phone, (509) 376-2378; fax, (509) 376-6767; e-mail, diana.bigelow@pnl.gov.

[1] Abbreviations: $C_{12}E_9$, polyoxyethylene 9 lauryl ether; CD, circular dichroism; FMal, fluorescein-5-maleimide; FTIR, Fourier transform infrared; MOPS, 3-(*N*-morpholino) propane-sulfonic acid; OG, *n*-octyl β-D-glucopyranoside; PKA, cAMP-dependent protein kinase; PLB, phospholamban; PLB_C, a single cysteine phospholamban with mutations of $Cys^{36, 41, 46}$ to Ala and Ala^{24} to Cys; P21A-PLB_C, PLB_C with an additional mutation of Pro_{21} to Ala; SERCA, Sarco(Endo)plasmic Reticulum Ca-ATPase; TCEP, Tris (2-carboxyethyl) phosphine hydrochloride.

10.1021/bi051075o CCC: $30.25 © 2005 American Chemical Society
Published on Web 11/11/2005

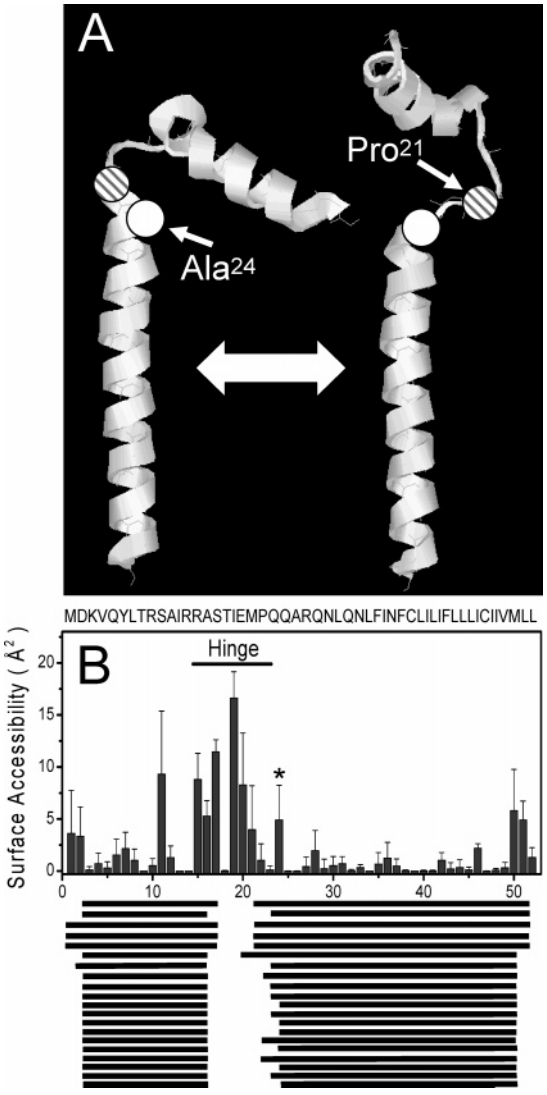

FIGURE 1: Depiction of interdomain hinge in PLB. (A) Three-dimensional molecular models of PLB show the variable interdomain hinge region in 2 of the 20 NMR structures (1N7L.pdb), depicting positions of Pro^{21} (striped circles) and Ala^{24} (white circles) (*47, 48*). (B) Variations in the calculated surface accessibilities (top) and secondary structures (bottom) are shown for all 20 NMR structures; position 24 associated with attachment of FMal is indicated (*). Bars represent average surface accessibilities of Cα carbons to molecular iodide (van der Waals radii of 2.15 Å) calculated using Surface Racer 1.1 (http://monte.biochem.wisc.edu/~tsodikov/surface.html) (*49*), where the variation between 20 structures is reflected in the error bars. Black rectangles below the figure represent regions of helical structure present in the family of 20 NMR structures.

which is linked to the large-scale structural transition associated with calcium activation and formation of the second calcium binding site (*2, 4*−*8*).

Recent atomic resolution structures of PLB obtained from NMR have provided new mechanistic insights regarding PLB regulatory function (*9*−*13*). For example, several monomeric forms of PLB in different solvents exhibit remarkable uniformity of structure, but also demonstrate a large degree of conformational heterogeneity apparent in the families of between 10 and 24 structures resolved for each NMR structure determination (Figure 1). These structures all consist of two α-helices connected by a β-turn, centered around the sequence $TIEMP^{21}$. Individual structures vary with respect to the length of individual helices as well as the angle between helical elements, which varies by approximately 40 degrees. Assuming a common orientation within the lipid bilayer of the C-terminal helix of these PLB structures, the observed heterogeneity represents variation in positioning of the N-terminal helix with respect to the bilayer surface, suggesting that the region around the β-turn acts as a flexible hinge that can accommodate different interactions with the Ca-ATPase (*11, 12*). The flexibility of this region has been confirmed by NMR measurements demonstrating highly dynamic amide backbone motions relative to other regions within PLB (*13*).

The location of phosphorylation sites at the interface of this flexible hinge further suggests that modulation of the hinge is critical to the regulation of PLB−ATPase interactions. Indeed, comparing NMR structures of the nonphosphorylated PLB peptide, corresponding to residues 1−36, with the same peptide phosphorylated at Ser^{16} and Thr^{17} indicates phosphorylation-dependent alterations to the average angle between N- and C-terminal helices, bringing portions of both helices into closer proximity (*9, 10*).

Therefore, in the present study, we asked if the flexible hinge observed from NMR structures of isolated PLB in solvents and micelles is relevant to the regulatory interactions of PLB when bound to the Ca-ATPase. Proline is present at the helix−coil interface within PLB; a proline at this position, commonly observed within a range of different protein structures, is known to impose structural constraints on the protein backbone. As a means to effectively alter the structure of the hinge region, Pro^{21} was mutated to an alanine, which, with its small side chain and lack of chemical reactivity, favors the formation of an α-helix. This mutation modifies the hinge structure of PLB, as evidenced by both circular dichroism and fluorescence spectral changes, that indicate increased α-helicity of PLB, decreased solvent accessibility of fluorescein 5-maleimide (FMal) at position 24, and an increase in the overall dimensions of the carboxyl-terminal domain apparent from measurements of rotational dynamics. These structural changes result in partial loss of inhibition of the Ca-ATPase by the mutant P21A-PLB_C, with no change in the extent of activation of the Ca-ATPase following phosphorylation of PLB by cAMP-dependent protein kinase (PKA). A consideration of the calcium dependence of ATPase activity and simulations of the Ca-ATPase steady-state reaction mechanism indicate that PLB selectively disrupts the cooperative structural transition associated with the formation of the second high-affinity calcium binding site by reducing the equilibrium constant from 2.0 (indicative of positive cooperativity) for the uninhibited enzyme to 0.5 (negative cooperativity) or 1.0 following association of either PLB_C or P21A-PLB_C with the Ca-ATPase. The diminished level of Ca-ATPase inhibition upon reconstitution of the Ca-ATPase with P21A-PLB_C in comparison to wild-type PLB indicates that an extended and flexible interhelical region facilitates PLB binding and the uncoupling of the cooperativity between the two high-affinity calcium binding sites of the Ca-ATPase.

EXPERIMENTAL PROCEDURES

Materials. Fluorescein-5-maleimide (FMal) was obtained from Molecular Probes, Inc. (Junction City, OR). Polyoxyethylene 9 lauryl ether ($C_{12}E_9$), cAMP-dependent protein

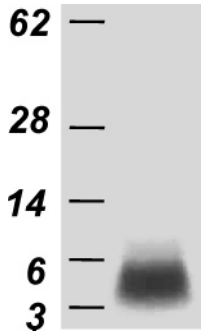

FIGURE 2: Electrophoretic mobility of P21A-PLB_C as a monomeric species. The P21A-PLB_C mutant exhibits electrophoretic mobility on a 4−12% gradient SDS−PAGE gel as a 6 kDa species, consistent with prior suggestions that mutation of transmembrane cysteines (i.e., Cys^{31}, Cys^{36}, and Cys^{41}) to alanines stabilizes the monomeric form of PLB (*17*). Molecular marker protein positions are from top to bottom: bovine serum albumin (62 kDa), carbonic anhydrase (28 kDa), lysozyme (14 kDa), aprotinin (6 kDa), and the B chain of insulin (3 kDa).

kinase (PKA), cAMP, ATP, $MgCl_2$, the calcium ionophore A23187, EGTA, DEAE-cellulose, and *n*-octyl β-D-glucopyranoside (OG) were purchased from Sigma (St. Louis, MO). 3-(*N*-morpholino) propane-sulfonic acid (MOPS) was purchased from Fisher Biotech (Fair Lawn, NJ). Bio-Beads SM2 was purchased from Bio-Rad (Richmond, CA). The Ca-ATPase was affinity-purified from rabbit fast-twitch skeletal muscle SR using reactive Red-agarose (*14*). Purified PLB and Ca-ATPase were stored at −70°C.

Expression and Purification of PLB. Cysteine null ($Cys^{36,41,46}$Ala) and single cysteine ($Cys^{36,41,46}$Ala/Ala^{24}Cys) PLB mutants, designated PLB_C and P21A-PLB_C were cloned into the pGEX-2T plasmid expression vector and expressed in JM109 *Escherichia coli* cells as previously described (*15*, *16*). Using overlap PCR to further generate the point mutation, Pro^{21} to Ala^{21}, on the single cysteine mutant PLB (PLB_C), we designed the forward primer (5′GAAATGGCT-CAACAAGCACGTC AAAAC 3′) and the reverse primer (5′ GTTTTGACGTGCTTGTTGAGCCATTTC3′) to contain the mutagenic site encoding alanine at position 21(underlined). The PCR-amplified products were subsequently subcloned into a pET15b plasmid expression vector (Novagen, Madison, WI). Positive clones were screened and verified by DNA sequencing (Amplicon Express, Pullman, WA) and transformed into JM109 *E. coli* strain for protein expression. The expressed PLB protein was purified by preparative electrophoresis, essentially as previously described (*14*), with the exception that (*i*) *E. coli* cells were lysed by incubation with 200 μg/mL lysozyme at room temperature prior to sonication and (*ii*) the resulting membrane pellet collected by centrifugation at 150 000*g* for 10 min was solubilized with 1% Sarkosyl in 20 mM Tris-HCl (pH 7.5) before isolation by preparative electrophoresis. Purified P21A-PLB_C migrates as a single band on SDS−PAGE (Figure 2), consistent with prior results that have established the 3C3A-PLB mutant to be a monomer in solution (*17*).

Co-Reconstitution of the Ca-ATPase with PLB. The Ca-ATPase was reconstituted in the absence or presence of PLB at a molar ratio of three PLB per Ca-ATPase into liposomes of extracted SR lipids as previously described (*18*). The concentration of PLB was determined by the Amido Black method (*19*).

Enzymatic, Protein, and Free Calcium Assays. ATP hydrolysis activity of the Ca-ATPase was determined at 25 °C by measuring the time course of the release of inorganic phosphate (*20*), using 100 μg of protein/mL in a solution containing 50 mM MOPS (pH 7.0), 0.1 M KCl, 5 mM $MgCl_2$, 1 mM EGTA, 1 μM CCCP, 2 μM valinomycin, 2 μM A23187, and sufficient calcium to yield the desired concentration of free calcium, adding 5 mM ATP to start the reaction (*18*). To phosphorylate PLB for enzyme activity measurements, 10 μg PKA/mL and 1 μM cAMP were included in the assay buffer; PLB was phosphorylated upon addition of ATP and initiation of the reaction mechanism. All protein concentrations were determined by the Amido-Black method (*19*). Free calcium concentrations were calculated from total ligand and EGTA concentrations, correcting for pH and ionic conditions (*21*).

Estimation of Cooperative Calcium Binding and Simulation of Calcium-Dependent Changes in Enzyme Activities. Calcium activation of the Ca-ATPase is a cooperative process, whereby the binding of the first calcium ion (step a) functions to induce a conformational transition (i.e., the formation of E′ in step b) that is associated with the formation of the second calcium binding site whose occupancy in step c leads to enzyme activation (i.e., Activity), as indicated by eq 1. K_a, K_b, and K_c represent the associated equilibrium

$$E + Ca^{2+} \overset{K_a}{\longleftrightarrow} E_{Ca} \overset{K_b}{\longleftrightarrow} E'_{Ca} + Ca^{2+} \overset{K_c}{\longleftrightarrow} E'_{Ca_2} \qquad (1)$$

constants for each reaction step. By explicitly taking into account the two intrinsic equilibrium constants associated with calcium binding (K_a and K_c), it is possible to determine whether PLB modulates the relative affinities and cooperative interactions between high-affinity calcium binding sites of the Ca-ATPase (as fully described by Shea and co-workers for calcium binding (*22*)) by fitting the activity data to the following equation:

$$\text{Activity} = \frac{K_1[Ca^{2+}]_{free} + 2K_2[Ca^{2+}]_{free}{}^2}{2(1 + K_1[Ca^{2+}]_{free} + K_2[Ca^{2+}]_{free}{}^2)} \qquad (2)$$

where $K_1 = K_a + K_c$ and $K_2 = K_aK_bK_c$. A lower limit of the true value associated with the cooperative structural transition K_b can be estimated by assuming $K_a = K_c$ where

$$K_b = \frac{4K_c}{K_a{}^2} \qquad (3)$$

Additional insight into PLB-dependent changes in the cooperativity between calcium binding sites and their relationship to steady-state ATPase activities involved the simulation of the complete reaction cycle of the Ca-ATPase using the Biological Modeler of the TERANODE design suite (http://www.teranode.com/products/tds/bioedition.php) and the published rate constants measured by Inesi and co-workers (*4*).

Circular Dichroism Measurements. Circular dichroism (CD) spectra were measured with an AVIV Model 60DS spectropolarimeter and a temperature-jacketed spectral cell with a path length of 0.5 cm. PLB spectra were recorded in 20 mM Tris (pH 7.0), 50 mM NaCl, and 0.1% $C_{12}E_9$ at 1-nm intervals between 202 and 260 nm. The mean residue molar

ellipticity, [θ], was calculated using the following formula:

$$[\theta] = \frac{\theta_{\text{measured}} \times 10^{-3}}{[\text{P}]nl} \quad (4)$$

where θ_{measured} is the measured ellipticity in millidegrees, [P] and n are the concentration (in decimoles per cubic centimeter) and the number of peptide bonds in PLB, respectively, and l is the path length of the CD cell. The molecular masses (M_r) are 5987 g/mol for PLB_C and 5961 g/mol for P21A-PLB_C. In all cases, the number of peptide bonds was 52. The apparent α-helical content of PLB was determined using the CDPro software package, which contains the programs SELCON3, CDSSTR, and CONTIN (http://lamar.colostate.edu/~sreeram/CDPro/). Each program uses a distinct algorithm for comparative analysis of the measured data with a reference data set (*23*). This approach provides increased reliability of the secondary structure analysis as results are only considered valid when the outputs of all three programs are comparable. The reference data set used for analysis consisted of 43 soluble proteins and 13 membrane proteins. The outputs of the three methods were equivalent, and reported values represent averaged values and a standard deviation that represents the variation between the models. In all cases, the variation between models exceeds that associated with sample preparation and CD measurements.

Derivatization of PLB with FMal. The chemical modification of the single Cys^{24} with FMal was carried out essentially as previously described (*24*). PLB (20 μM) was incubated in 200 μM TCEP (Pierce, Rockford, IL), 0.1% $C_{12}E_9$, 20 mM Tris (pH 7.3), and 50 mM NaCl for 2 h at room temperature prior to the addition of less than 2% vol of FMal from a stock solution in DMSO at a final concentration of 200 μM. This reaction mixture was incubated for 12 h at 25 °C. Unreacted FMal was removed using a Sephadex G-15 size-exclusion column, eluting with 0.1% $C_{12}E_9$, 20 mM Tris buffer (pH 7.0), and 20 mM NaCl. Molar stoichiometries of FMal to PLB were measured from the ratio of the dye concentration, measured from the fluorescein extinction coefficient, $M_{492} = 83\,000\ \text{cm}^{-1}\ \text{M}^{-1}$, and the PLB concentration from the Amido-Black protein assay. Final molar stoichiometries of FMal per PLB for the samples used in this study were 1.0 ± 0.1.

Steady-State Fluorescence Measurements. Steady-state fluorescence spectra were measured using a Fluoromax-3 spectrofluorometer (Jobin Yvon Spex; Edison, NJ). Protein conformational changes were assessed by changes in the accessibility of bound FMal to the soluble quencher of fluorescence, iodide, involving measurements of fluorescence intensity of FMal as a function of quencher concentration. FMal was excited at 492 nm for measurement of emission at 518 nm; slit widths were 5 nm. The resulting data were plotted as F_0/F as a function of the titrated iodide concentration and according to the Stern−Volmer equation:

$$F_0/F = 1.0 + K_{SV}[\text{Q}] = 1.0 + k_q\langle\tau\rangle[\text{Q}] \quad (5)$$

where, F_0 and F are the fluorescence intensity in the absence and presence of iodide, respectively. [Q] represents the concentration of quencher, iodide, added as KI. K_{SV} is the slope of a linear fit to the data, that is, the Stern−Volmer quenching constant, which is the product of both the average fluorescence lifetime in the absence of quencher (i.e., $\langle\tau\rangle$) and the bimolecular quenching constant (k_q), the true measure of solvent accessibility.

Measurement and Analysis of Frequency-Domain Data. Frequency domain data (lifetime and anisotropy) were measured using an ISS K2 frequency domain fluorometer (ISS Inc., Champaign, IL), as described previously (*25*). Fluorophore excitation used the 476 nm output from a Coherent (Santa Clara, CA) Innova 400 argon ion laser; emitted light was collected after a 3rd Millenium 540 nm long-pass filter (Omega Opticals, Brattleboro, VT), using glycogen in water as a scattering reference. Measurements were made at 22 °C. Explicit expressions, previously described in detail, permit the ready calculation of the lifetime components (i.e., α_i and τ_i) relating to a multiexponential decay of FMal (*25*). Algorithms are available that permit the determination of the initial anisotropy in the absence of rotational diffusion (r_o), the rotational correlation times (φ_i), and the amplitudes of the total anisotropy loss associated with each rotational correlation time ($r_0\ g_i$), as previously described in detail (*26*, *27*). The parameter values are determined using the method of nonlinear least-squares analysis in which the reduced chi-squared (i.e., χ_R^2) are minimized (*28*). A comparison of χ_R^2 values provides a quantitative assessment of the adequacy of different assumed models to describe the data (*29*). Data were fit using the Globals software package (University of Illinois, Urbana-Champaign, IL) or Vinci Analysis (ISS Inc., Champaign, IL).

RESULTS

Generation and Rationale of PLB Mutants. A PLB mutant was genetically engineered in which Pro^{21} was substituted with an alanine (i.e., P21A-PLB_C), which is predicted to alter the flexible hinge of PLB by introducing an amino acid compatible with helix formation and thus disrupting the adjacent β-turn (*30*). To avoid complexities resulting from self-association, all PLB mutants were made on a cysteine-null background, in which the three transmembrane cysteines, Cys^{36}, Cys^{41}, and Cys^{46} of wild-type PLB were replaced by alanines. As previously reported, these alterations stabilize the functional form of PLB by disrupting noncovalent intermolecular interactions that favor the formation of pentamers in wild-type PLB (*17*). PLB species used in the present study include (*i*) a single cysteine mutant, in which Ala24 is replaced with a cysteine to permit thiol-directed fluorophore derivatization, designated PLB_C, and (*ii*) this single cysteine PLB with an additional mutation of Pro^{21} to Ala, designated P21A-PLB_C. In both samples, the location of a thiol-reactive moiety for the site-specific labeling of PLB at position 24 with FMal was motivated by prior structural data (*24*), which suggested that the surface accessibility at position 24 would be sensitive to changes in PLB secondary structure (Figure 1).

Functional Effects of Pro21Ala Mutation in PLB. Coreconstitution of PLB with the SR Ca-ATPase in liposomes results in a shift in the calcium concentration dependence of enzymatic activation toward higher calcium concentrations relative to that of Ca-ATPase alone (Figure 3). Coreconstituted PLB_C provides inhibition of the Ca-ATPase that

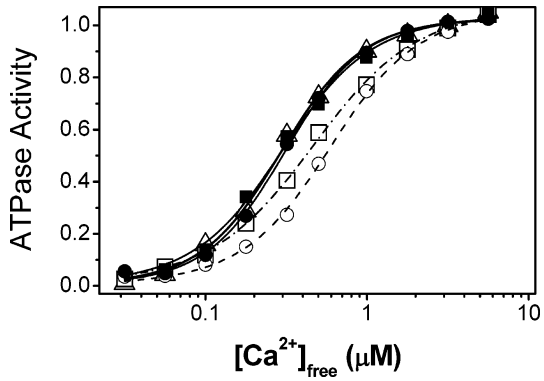

FIGURE 3: Diminished inhibition of Ca-ATPase by PLB upon P21A mutation. Calcium dependence of ATPase activity for the Ca-ATPase reconstituted into liposomes in the absence of PLB (△), the presence of PLB_C (○; ●), and the presence of P21A-PLB_C (□; ■). The calcium dependence of ATPase activity after phosphorylation of PLB by PKA (see Experimental Procedures for details) is shown for PLB_C (●) or P21A-PLB_C (■). Calcium concentrations associated with half-maximal activation of the Ca-ATPase and Hill coefficients (fits not shown) are 290 ± 10 and 1.69 ± 0.09 nM (△), 580 ± 20 and 1.53 ± 0.07 nM (○), 310 ± 10 and 1.74 ± 0.08 nM (●), 460 ± 20 and 1.3 ± 0.04 nM (□), and 300 ± 10 and 1.51 ± 0.08 nM (■). The maximal Ca^{2+}-dependent ATPase activity was 2.8 ± 0.2 μmol of P_i·mg $^{-1}$·min^{-1} at 24 °C. Curves were obtained from a least-squares fit to eq 1; the resulting parameters are shown in Table 1.

is equivalent to that observed for wild-type PLB in native SR, as evidenced by the 290 ± 10 nM shift in the [Ca^{2+}] of half-maximal activation ($Ca_{1/2}$) from 290 ± 10 nM, for Ca-ATPase alone, to 580 ± 20 nM for Ca-ATPase with PLB_C (*16*, *18*, *24*, *31*−*33*). Phosphorylation of reconstituted PLB_C by PKA results in full reversal of Ca-ATPase inhibition as evidenced by its nearly identical calcium activation curve as compared with that of the Ca-ATPase reconstituted in the absence of PLB. In contrast, the Ca-ATPase co-reconstituted with P21A-PLB_C exhibits only partial inhibition of Ca-ATPase activity, having a $Ca_{1/2}$ value of 460 ± 20 nM. Moreover, the activity of the Ca-ATPase reconstituted with P21A-PLB_C exhibits diminished cooperativity, as evidenced by fitting the activity data to a model which explicitly addresses the relative affinities and cooperative interactions between high-affinity calcium binding sites of the Ca-ATPase (*22*) (Table 1). Co-reconstitution of the Ca-ATPase in the presence of P21A-PLB_C results in a 0.6 kcal mol^{-1} reduction in the cooperativity (K_c) between calcium binding sites relative to that of PLB_c. This latter effect of reconstituted PLB_C is in good agreement with the reduced cooperativity between calcium binding sites of the Ca-ATPase observed in cardiac SR as compared with that after PKA phosphorylation of PLB. Thus, wild-type and PLB_C appear to modulate the cooperative structural transitions between the two high-affinity calcium binding sites of the Ca-ATPase (*4*).

Replacement of Pro^{21} with Ala Induces Increased Helicity in PLB. Circular dichroism (CD) measurements were used to compare the secondary structure of PLB_C with that of P21A-PLB_C to test the hypothesis that the loss of Pro^{21} will disrupt the β-turn of the hinge region, resulting in increased helical content. The CD spectrum for PLB_C, as well as that for the cysteine null PLB mutant, exhibits nearly identical spectra with well-defined minima at 207 and 222 nm characteristic of substantial α-helical content (Figure 4), consistent with prior CD measurements for PLB cysteine-null mutants (*34*). In comparison to PLB_C, the spectrum for the P21A-PLB_C mutant exhibits diminished ellipticity, indicating a larger α-helical content relative to PLB species with proline at position 21. The spectra were fit using three different algorithms (SELCON3, CDSSTR, and CONTIN) for comparing measured data with reference data sets, providing estimates of secondary structure content (Table 2). Equivalent results were obtained from all three methods, indicating the reliable prediction of secondary structures of these PLB mutants. These models provide good fits to the measured ellipticities as illustrated by the randomly distrib-

Table 1: Free Energy Changes Associated with Calcium Activation of the Ca-ATPase Reconstituted in the Absence and Presence of PLB_c and P21A-PLB_C[a]

sample	ΔG_1 (kcal/mol)	ΔG_2 (kcal/mol)	ΔG_b [c] (kcal/mol)
Ca-ATPase alone	−8.4 ± 0.1	−17.8 ± 0.1	−1.9 ± 0.3
+ PLB_c	−8.1 ± 0.1	−17.0 ± 0.1	−1.6 ± 0.3
+ PLBc and PKA	−8.3 ± 0.2	−17.7 ± 0.1	−2.0 ± 0.3
+ P21A-PLB_c	−8.6 ± 0.1	−17.4 ± 0.1	−1.0 ± 0.2
+ P21A-PLB_c and PKA	−8.3 ± 0.2	−17.8 ± 0.1	−2.0 ± 0.3
Native SR Vesicles			
skeletal SR (Ca-ATPase alone)[b]	−8.4 ± 0.2	−18.1 ± 0.1	−2.1 ± 0.2
cardiac SR (+ PLB)[b]	−8.1 ± 0.1	−16.9 ± 0.1	−1.5 ± 0.1
cardiac SR +PKA (+PLB and PKA)[b]	−8.3 ± 0.3	−17.8 ± 0.1	−2.0 ± 0.3

[a] Values represent free energy values derived from the equilibrium constants from a nonlinear least-squares fit of the data shown in Figure 3 using eq 2 in Experimental Procedures. [b] Values taken from the previous study of native SR (Figure 1, Table 1) (*44*). [c] Estimation of lower limit of cooperative free energy was calculated as follows: $\Delta G_b = -0.82$ kcal/mol + $\Delta G_2 - 2\Delta G_1$, as previously described (*22*).

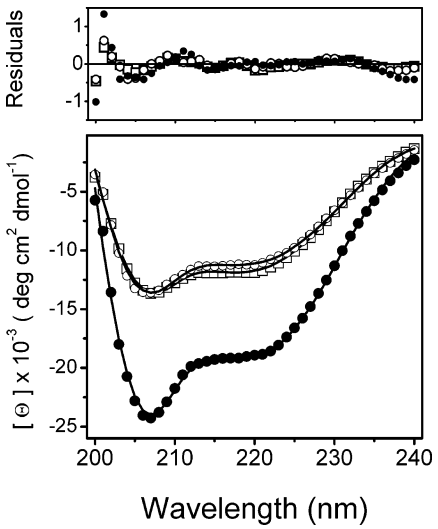

FIGURE 4: Increased helical structure in P21A-PLB. Circular dichroism (CD) spectra data points are shown for P21A-PLB_C (●) compared with PLB_C (○) or the cysteine-null PLB (□) over the wavelength range of 200−250 nm (lower panel). Solid lines represent the fits of each data set to the CD analyses algorithm CONTIN; the upper panel illustrates the weighted residuals (i.e., the difference between the experimental data and the calculated fit for each sample). Depicted spectra were corrected for background absorption from the buffer and were obtained using approximately 0.2 μg PLB/mL in 20 mM Tris (pH 7.0), 50 mM NaCl, and 0.1% $C_{12}E_9$ at 25 °C. Measurements were made using a sample cell with a 0.2 mm path length cell in an AVIV model 62DS CD spectrometer; each data point is the average of three spectral scans with four different measurements at each wavelength.

Table 2: Secondary Structure Content Estimated from CD Spectra[a]

sample	α-helix	β-sheet	turn	unstructured
P21A-PLB$_C$	0.57 ± 0.06	0.07 ± 0.02	0.11 ± 0.03	0.25 ± 0.02
PLB$_C$	0.34 ± 0.02	0.16 ± 0.01	0.20 ± 0.01	0.30 ± 0.01
Cys-null PLB	0.33 ± 0.02	0.17 ± 0.01	0.20 ± 0.01	0.30 ± 0.01

[a] The average fraction of secondary structural content (α-helix, β-sheet, turn, and unstructured) is represented; each value represents the mean value of structural content determined from fitting the CD spectra for each individual sample to three different algorithms (CONTIN, SELCON3, and CDSSTR) (http://lamar.colostate.edu/~sreeram/CDPro/). Standard deviations of average values from the three models are also indicated.

uted residuals shown for one model and the small variance between models (Figure 4; Table 2) (*23*).

There are substantial increases in helical content upon replacement of Pro[21] with Ala, with associated decreases in nonhelical content derived primarily from β-structure (Table 2). The calculated helical content of PLB$_C$ and the Cys-null PLB is 33 ± 2% and 34 ±2%, respectively, while the helical content of P21A-PLB$_C$ increases to 57 ± 6% (Table 2). Although available NMR structures of PLB show significantly higher helical contents, consistent with the preference of NMR for ordered structures, considerable variability is present in these structures. For example, in the C41F PLB structure (*11*), 34 amino acids appear in nonhelical conformations in one or more of the resolved structures, with the remaining 35% of the amino acid sequence exhibiting α-helical conformations in all structures. In particular, amino acids within a 15 residue window (residues 9−23) centered around the hinge region commonly appear in nonhelical conformations. Thus, the 23 ± 7% increase in helical content of P21A-PLB$_C$ relative to PLB$_C$ could be explained by the transformation of 12 ± 4 of these amino acids to a stable helix.

Local Structural Changes Probed at Cys[24] of PLB. To assess the effect of the alanine replacement of Pro[21] specifically on the structure of the hinge region, Cys[24] in the engineered PLB mutants was derivatized with the fluorophore, FMal. This labeling site was engineered near the helix−turn interface in the high-resolution NMR structures of PLB in a region whose surface accessibility is highly variable between reported NMR structures in correspondence with alterations in the helical content of this sequence (Figure 1B). Furthermore, this position has previously been shown to be sensitive to phosphorylation-induced structural changes within the hinge region that function to modulate the structural coupling between the opposing helical elements of PLB (*24*). FMal bound to P21A-PLB$_C$ exhibits decreased accessibility to the soluble quencher, iodide, relative to that of PLB$_C$, as evidenced by the decrease in the slope (K_{SV}) of the Stern−Volmer plot (Figure 5). As the measured K_{SV} is the product of both solvent accessibility and fluorescence lifetime of the fluorophore, lifetimes of FMal bound to both PLB$_C$ and P21A-PLB$_C$ were measured to ask if the different slopes of the Stern−Volmer plots reflect true differences in solvent accessibility. Frequency domain fluorescence measurements of the decay times of bound FMal indicate virtually identical lifetimes for this fluorophore bound to mutant or PLB$_C$ (Figure 6; Table 3). Thus, differences in measured K_{SV} values accurately reflect differences in the solvent accessibility of bound FMal, and are consistent with

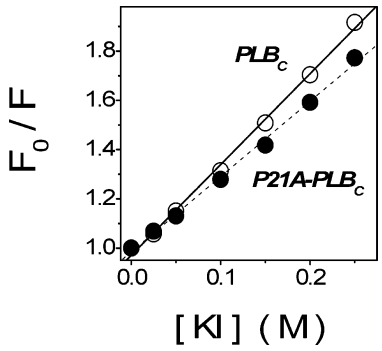

FIGURE 5: Structural change near hinge element in P21A-PLB. Collisional quenching of FMal bound to Cys[24] was used to measure solvent accessibility for PLB$_C$ (○) and P21A-PLB$_C$ (●). Quenching was measured as the fluorescence intensity (F) relative to that of the unquenched sample (F_0) at various iodide concentrations. The slopes of a linear fits to the data, i.e., the Stern−Volmer constants (K_{SV}), are 3.69 ± 0.09 and 3.06 ± 0.08 M^{-1}, respectively, for PLB$_C$ and P21A-PLB$_C$. PLB samples were measured in 20 mM Tris (pH 7.0), 50mM NaCl, and 0.1% $C_{12}E_9$ at 25 °C. Fluorescence was measured at 518 nm with excitation at 492 nm using 5 nm slit widths. Data points represent the means of four separate measurements.

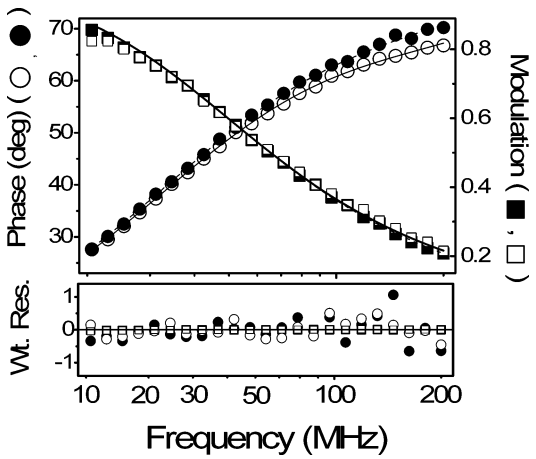

FIGURE 6: Frequency domain lifetime data for FMal bound to PLB$_C$ and P21A-PLB$_C$. Upper panel depicts frequency−response data (symbols) corresponding to the phase shift (●, ○) and modulation (■, □), and corresponding two-exponential fits (solid line, dashed line) are shown for FMal-labeled P21A-PLB$_C$ (●, ■) and FMal-labeled PLB$_C$ (○, □). Lower panel illustrates weighted residuals (i.e., the difference between the experimental data and the calculated fit divided by the experimental uncertainty of individual measurements). Experimental conditions involved 0.2 μg/mL of PLB in 20 mM Tris (pH 7.0), 50 mM NaCl, and 0.1% $C_{12}E_9$ at 22 °C.

a more structured environment in the hinge region as a result of the P21A mutation. Thus, observed decreases in the solvent accessibility of FMal at position 24 in P21A-PLB$_C$ is consistent with the CD measurements, indicating greater helical content in this mutant, and supports models that suggest the helical content of the dynamically disordered hinge structure is stabilized upon mutation of P21A.

Diminished Mobility of the C-Terminal Domain in P21A-PLB$_C$. Frequency domain fluorescence anisotropy measurements of the rotational dynamics of FMal-PLB$_C$ permit an understanding of how the Pro[21]Ala mutation affects the overall dimensions of the C-terminal domain of PLB. To measure the rotational dynamics, the differential phase and modulated anisotropy of FMal bound to P21A-PLB$_C$ and to PLB$_C$ were measured over 40 frequencies between 2.5 and

Table 3: Lifetime Data for FMal Covalently Bound to Cys[24] within PLB_C and P21A-PLB_C[a]

sample	α_1	τ_1 (ns)	α_2	τ_2 (ns)	χ^2_R	$\langle\tau\rangle$[b] (ns)	k_q[c] $\times 10^{-9}$ (M^{-1} s^{-1})
PLB_c	0.09 ± 0.01	0.6 ± 0.1	0.91 ± 0.010	4.4 ± 0.1	4.6	4.3 ± 0.1	0.86 ± 0.02
P21A-PLB_C	0.07 ± 0.01	0.7 ± 0.1	0.93 ± 0.01	4.4 ± 0.1	6.6	4.4 ± 0.1	0.70 ± 0.02

[a] Average terms (α_i) and lifetimes (τ_i) obtained from two-exponential fits to frequency domain data for the time-dependent intensity decay, $\alpha(t)$, for FMal bound to Cys24 in PLB, assuming $\alpha(t) = \sum_i \alpha_i \exp(-t/\tau_i)$. Frequency domain data was measured under conditions described in Figure 6. [b] $\langle\tau\rangle = \sum_i \alpha_i \tau_i 2 / \sum_i \alpha_i \tau_i$. Errors represent the standard errors of the mean for three independent measurements. [c] Bimolecular quenching coefficient determined from the slopes of linear fits to the data in Figure 5, from the equation, $K_{SV} = k_q(\tau_0)$, where K_{SV} is the Stern−Volmer quenching constant, i.e., the slope of quenching data as in Figure 5 and τ_0 is the lifetime of the fluorophore in the absence of quenching.

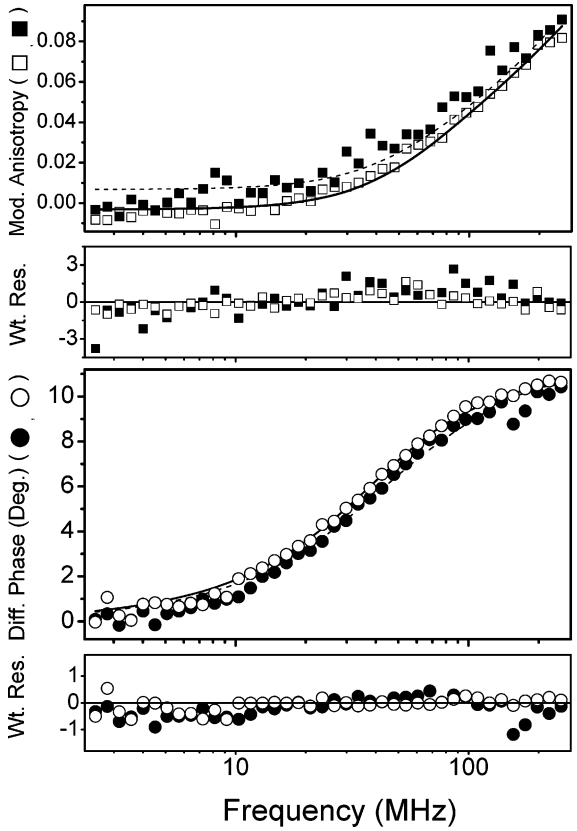

FIGURE 7: Rotational dynamics of PLB. Measured differential phase angles (○, ●) and modulated anisotropy (□, ■) for FMal-labeled PLB_C (○, □) and P21A-PLB_C (●, ■) in 20 mM Tris (pH 7.0), 50 mM NaCl, and 0.1% $C_{12}E_9$ at 22 °C. Nonlinear least-squares fits to a model involving two rotational correlation times corresponding to probe mobility (φ_1) and the overall domain motion (φ_2) are shown for PLB_C (solid line; $\varphi_1 = 0.5 \pm 0.1$ ns, $\varphi_2 = 4.7 \pm 0.3$ ns) and P21A- PLB_C (dashed line; $\varphi_1 = 0.6 \pm 0.1$ ns, $\varphi_2 = 6.2 \pm 0.8$ ns). Lower panels below respective data sets represent the weighted residuals (i.e., the difference between the experimental data and the calculated fit divided by the experimental uncertainty).

250 MHz (Figure 7). Similar frequency responses are observed for the differential phase and modulated anisotropy irrespective of the Pro[21]Ala mutation, consistent with the fact that both mutants are monomeric in solution. Nevertheless, there are significant differences, such that in comparison to PLB_C the modulated anisotropy of P21A-PLB_C is consistently higher, while the differential phase is shifted toward higher frequencies. Consistent with observed qualitative changes in the frequency response, a nonlinear least-squares fit of the data to determine the rates of motion associated with the C-terminal domain of PLB indicates that there are two rates of motion whose relative amplitudes are essentially unchanged. The shorter rotational correlation time (i.e., $\varphi_1 = 0.5$ ns), corresponding to the independent motion of the probe, is essentially unchanged by mutation of Pro[21] to Ala. In contrast, the longer rotational correlation time associated with domain motion increases from 4.7 ± 0.3 ns for PLB_C to 6.2 ± 0.8 ns for P21A-PLB_C which is statistically significant, as judged by the lack of overlap in the error surfaces in a rigorous analysis of correlated errors in the fit to the data (Figure 8). The increase in the rotational correlation time of P21A-PLB_C is indicative of an increase in the overall dimensions of the C-terminal domain of PLB.

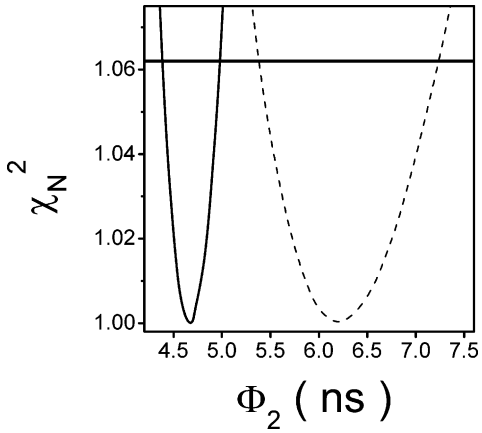

FIGURE 8: P21A mutation induces an expanded structure of the carboxyl-terminal domain of PLB. Depiction of error surfaces for rotational mobility of carboxyl-terminal domain of PLB_C (solid line) and P21A-PLB_C (dashed line) measured using FMal bound to Cys-24. Normalized χ^2_N values were determined from nonlinear least-squares fits to the data depicted in Figure 7 following incremental adjustment of the rotational correlation time (Φ_2), essentially as previously described (*50*). The horizontal line at $\chi^2_N = 1.062$ corresponds to the *F*-statistic, which represents one standard deviation relative to the best fit to the data. Experimental conditions are as described in the legend to Figure 7.

An appreciation of the structural differences associated with the mutation of Pro[21] to Ala is possible from a consideration of the expected rotational dynamics for the C-terminal helix in PLB in association with $C_{12}E_9$ within a micelle of diameter assumed to be approximately 20 Å. A rotational correlation time of 4.7 ± 0.3 ns observed for PLB_C is consistent with a C-terminal helix with a length of 42 ± 2 Å (approximately 27 ± 1 amino acids), in agreement with the prior NMR structures where approximately 29 amino acids are present in a continuous helix with a length of approximately 40 Å (*12*). In contrast, a rotational correlation time of 6.2 ± 0.8 ns observed for P21A-PLB_C requires that the C-terminal helix assumes a length of 50 ± 4 Å (approximately 32 ± 5 amino acids within an α-helix), suggesting that the P21A mutation results in an increase of 8 ± 5 Å or 5 ± 3 amino acids.

Taken together, these results indicate that the mutation Pro[21] to Ala in PLB stabilizes the helical content of the

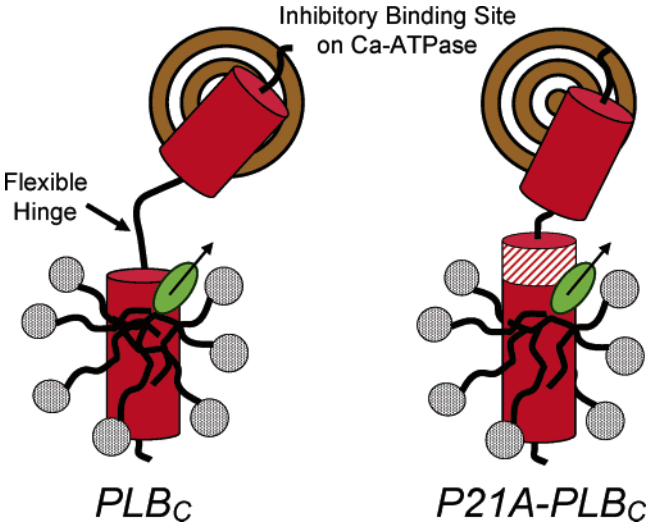

FIGURE 9: Model depicting disruption of inhibitory interaction between PLB and the Ca-ATPase upon stabilization of helical structure in hinge region of PLB. Average helical structures of C-terminal membrane spanning helix in $C_{12}E_9$ micelles and N-terminal cytosolic domain are shown as red cylinders, with random structure depicted as solid lines. Position of Cys24 and associated FMal label is depicted as a green oval with arrow. Left panel, flexible hinge between helical domain elements in PLB_C permits the N-terminal cytosolic helix to assume an extended structure, previously shown to be necessary for the productive association with inhibitory sequence Lys-Asp-Asp-Lys-Pro-Val[402] (bullseye) in the N-domain of the Ca-ATPase necessary for enzyme inhibition (*35*, *36*). Right panel, extension of C-terminal helix in P21A-PLB_C (red candy stripe) results in a shortening of the flexible hinge element, requiring some disruption of the inhibitory interaction between the N-terminal helical domain and the inhibitory sequence of the Ca-ATPase.

carboxyl-terminal domain, resulting in a reduction of the overall dimensions of the interdomain linker of PLB. This structural transition, in which the interdomain linker assumes a greater helical structure, functions to couple the carboxyl- and amino-terminal domains of PLB to modulate inhibition of the Ca-ATPase (Figure 9). The latter result is consistent with prior measurements that suggested a functional role for phosphorylation of Ser[16] in stabilizing the helical content of the interdomain linker in PLB to reduce the overall dimensions of PLB (*33*). Further, because inhibition of the Ca-ATPase requires PLB to assume an extended structure, these results suggest a model in which the modulation of the interdomain linker functions as part of a conformational switch to modulate the inhibition of the Ca-ATPase.

DISCUSSION

The location of Pro[21] at the interface of the β-turn and the C-terminal helix of PLB is consistent with the putative role of prolines as helix initiators, their infrequent occurrence within helices, and their common occurrence within β-turns (*30*). Thus, Pro[21] has been suggested to play a critical role in the maintenance of the flexible hinge of PLB (*11*, *12*). The prediction that replacement of Pro[21] with Ala will permit helix formation at the expense of the turn is supported by the CD spectral features of P21A-PLB_C indicative of increased helical content relative to PLB_C (Figure 4, Table 2). The $23 \pm 7\%$ increase in helical content suggests that there is an additional 12 ± 4 amino acids that assume a helical conformation. That this increased helical content occurs within the flexible hinge is supported by fluorescence changes reported by FMal covalently attached at Cys[24]. Previous measurements using the environmentally sensitive fluorophore, 2-(3′-maleimidylanilino) naphthalene-6-sulfonic acid (ANSmal), covalently bound to Cys[24] has indicated that this site is located outside the membrane and is sensitive to conformational changes induced by phosphorylation at Ser[16] (*24*). In the present study, FMal at this site exhibits mutation-induced local structural changes, as evidenced by its decreased solvent accessibility (Figure 5). Analysis using hydrodynamic theory of the measured rotational correlation times of bound FMal suggests that the C-terminal helix, to which FMal is attached, is extended by 8 ± 5 Å for P21A-PLB_C relative to that of PLB_C, which would correspond to an additional 5 ± 3 amino acids (Figures 7 and 8). This latter results is not statistically different from estimates using CD spectroscopy (12 ± 4 amino acids) and indicates an average extension of approximately eight amino acids. Thus, the effect of replacing Pro[21] with Ala is to lengthen the C-terminal helix at the expense of the flexible hinge, effectively shortening the "reach" of the cytosolic sequence of PLB (Figure 9). As a result of these structural changes, P21A-PLB_C makes less effective inhibitory interactions with the Ca-ATPase as evidenced by the decreased shift in the calcium activation curve of Ca-ATPase reconstituted with the mutant PLB (Figure 3).

The decreases in the solvent accessibility of FMal bound to Cys24 in the P21A-PLB_C mutant measured by CD spectroscopy strongly suggests that the helical content is stabilized near this reporter, in analogy to the low surface accessibility calculated for stable helical regions of PLB, in particular the C-terminal helix (Figure 1B). Our conclusion that the observed increase in overall helical content for P21A-PLB_C relative to PLB_C is largely due to helix formation within the hinge domain, is consistent with the NMR structure of PLB (1N7L.pdb), showing that the majority of the disordered structure is associated with PLB within this hinge domain. This interpretation is further supported by frequency domain anisotropy measurements that resolve rapid independent motions of this probe (i.e., 0.5 ns) from the overall motion of the C-terminal domain. The measured rotational correlation time corresponding to the C-terminal helix (i.e., 4.7 ± 0.3 ns) for PLBc is consistent with NMR structural data, which suggests that the C-terminal helix of PLB comprises about 29 amino acids. Indeed, calculations of the hydrodynamic properties of PLB based on this rotational correlation time indicate that the C- and N-helices are structurally uncoupled, consistent with prior FRET measurements (*16*, *32*, *33*). In the P21A PLB mutant, the rotational correlation time increases to 6.2 ± 0.8 ns. Since the C-helix undergoes independent motion relative to that of the N-domain, these results indicate that the overall dimensions of the C-helix increase. To estimate the extent of the conformational change, we have used the increase in the rotational correlation time to calculate the increase in overall dimensions of the helix, which indicates that the overall dimensions of the helix increase by approximately eight amino acids.

Information regarding the sites of physical proximity between PLB and the Ca-ATPase has been obtained from chemical cross-linking studies. For example, amino acids that span the length from the lumen to the top of the cytosolic

N-domain of the Ca-ATPase (positions 402, 321, 318, and 89) have been cross-linked with respective sites that span the length of PLB (residues 3, 27, 30, and 49) (*35*−*39*). These experimentally derived sites of proximity do not allow the available structures of PLB and SERCA to be fit together in silico, demonstrating that conformational changes to either or both proteins, relative to the crystal or NMR structures currently available, must occur for functional association of PLB with the Ca-ATPase (*39*, *40*).

The nature of these conformational changes has been suggested by several spectroscopic studies that have allowed unique detection of one protein in the presence of another. For example, FTIR measurements of isotopically labeled [^{13}C]PLB reconstituted with unlabeled Ca-ATPase permit the resolution of amide I and amide II absorbance bands of the Ca-ATPase distinct from those of ^{13}[C]PLB. These measurements indicate that PLB does not undergo large changes in secondary structure upon association with the Ca-ATPase, whereas the Ca-ATPase accommodates PLB with increased α-helical stabilization (*41*). An additional series of studies have involved time-resolved fluorescence resonance energy transfer (FRET) measurements to monitor the conformation of PLB with a donor−acceptor pair covalently modifying Tyr^6, on the N-terminal helix, and Cys^{24}, on the C-terminal helix, of PLB (*16*, *32*, *33*). These FRET measurements in the absence of the Ca-ATPase indicate a broad Gaussian distribution of distances, in good agreement with the average distances and conformational heterogeneity observed in NMR structures of PLB (*9*−*13*). In contrast, co-reconstitution of PLB with the Ca-ATPase results in a unique and highly ordered PLB conformation, as evidenced by the narrow (∼4 Å) distance distribution between donor−acceptor probes. The average distance between probes of 15 Å (or 14 Å when PLB is phosphorylated) is consistent with the analogous distances between side chains at positions 6 and 24 within NMR structures of PLB (*11*, *12*). However, this distance is inconsistent with models of the PLB−ATPase complex in which PLB is extended by helical unwinding to 22 or 30 Å in order to accommodate sites of cross-linking on the SERCA1 crystal structures (*38*, *39*). Thus, these direct structural measurements of PLB, in complex with the Ca-ATPase, suggests that the Ca-ATPase, rather than PLB, undergoes spatial reorientation of the N-domain to accommodate interaction with PLB. Indeed, reorientation of the nucleotide (N) domain has been measured in response to the phosphorylation of PLB, suggesting that altered protein interactions are involved in the phosphorylation-dependent loss of PLB inhibition of the Ca-ATPase (*42*). Phosphorylation of PLB at Ser^{16} by PKA also induces a small decrease in distance between donor−acceptor probes within PLB, at Tyr^6 and Cys^{24}, consistent with the suggested formation of a salt bridge between the phosphoryl group and Arg^{13} with stabilization of helix within this region. This small shortening of the N-terminal helix is sufficient to pull PLB away from its sites of optimal inhibitory interaction with the Ca-ATPase.

These inhibitory interactions of PLB conferred on active calcium transport may occur through the inhibition of catalytically important motions associated with the N-domains of the Ca-ATPase, which has been demonstrated to undergo calcium-dependent changes in mobility that effectively couple nucleotide hydrolysis to the formation of the covalent phosphoenzyme intermediate required for

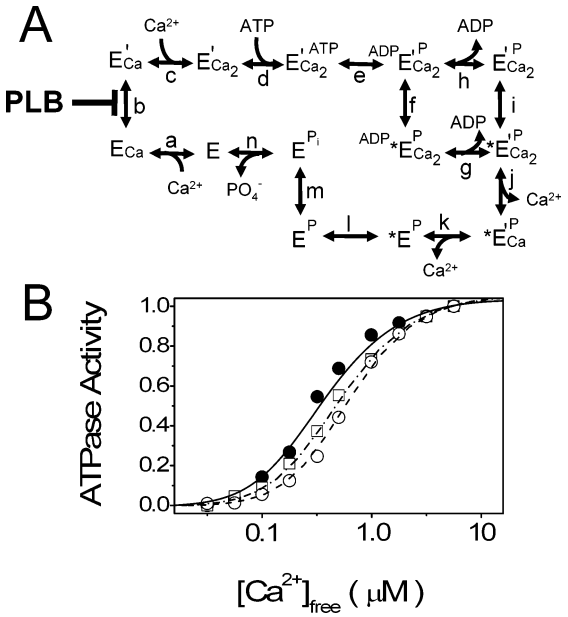

FIGURE 10: Simulation of calcium dependence of Ca-ATPase activity by PLB. Reaction scheme (A) and simulations (B) for calcium-dependent ATPase activity for the Ca-ATPase in the presence of PLB_C (●, ○) and P21A-PLB_C (□) either prior to (○, □) or following (●) activation by PKA. Rate constants for the simulation were obtained from Inesi and co-workers (*4*). Simulation of PLB inhibition was achieved by reducing the equilibrium constant for step b from 2.0 for the Ca-ATPase following release of PLB inhibition by PKA (●) to either 0.5 (○) or 1.0 (□) for the Ca-ATPase in the presence of PLB_C and P21A-PLB_C, respectively. Symbols represent experimental data shown in Figure 3, while curves represent the results of the kinetic simulations. Ligand concentrations are as defined in the legend to Figure 3.

calcium transport (*2*, *5*). Indeed, the PLB-dependent shift in the calcium-dependence of Ca-ATPase activity can be simulated by alteration of the equilibrium constant for a single reaction step, that is, the calcium-dependent formation of the second high-affinity calcium binding site (reaction b in Figure 10). The PLB-induced shift can be simulated by a 75% reduction in $K_{b,}$ from 2.0 (for Ca-ATPase alone), indicative of positive cooperativity, to 0.5 (for Ca-ATPase with PLB_C), indicative of negative cooperativity. Similarly, the diminished inhibition of Ca-ATPase activity by P21A-PLB_C can be simulated by a 50% reduction in the K_b. Utilizing the rate constants provided by Inesi and co-workers for the activated enzyme (corresponding to the Ca-ATPase in the absence of PLB) (*4*), we are able to simulate the calcium dependence of the Ca-ATPase activity only by floating rate constants associated with step b; alterations in no other reaction steps permit simulation of the experimental data. The best fit for the fully activated enzyme involved forward (k_f) and reverse (k_r) rate constants of 250 s^{-1} and 125 s^{-1}, respectively ($K_b = k_f/k_r = 2$). Thus, the Ala substitution for Pro^{21} within PLB has specific effects on the single-reaction step representing the conformational change of the Ca-ATPase that links the high-affinity binding of the first calcium with the formation of the second high-affinity calcium binding site, consistent with the observed changes in the cooperativity of calcium activation (Table 1).

These results are comparable to earlier measurements by Inesi and co-workers, which demonstrated that PLB binding shifts the calcium dependence of Ca-ATPase activation toward higher calcium concentrations as a result of a kinetic

effect involving the calcium-dependent activation of the enzyme (*4*). In these studies, equilibrium calcium binding measurements demonstrated that following addition of an antibody against PLB, which simulates the activation observed with PLB phosphorylation, there are no changes in the calcium affinity of the ATPase. Rather, the increased calcium sensitivity of the Ca-ATPase was simulated by small changes in the rate constants associated with calcium activation, indicating that the cooperative transition associated with the formation of the second high-affinity calcium binding site on the Ca-ATPase can explain the large change in the calcium sensitivity of the Ca-ATPase. From this model, a satisfactory simulation was possible by simply increasing both the forward and reverse rate constants 10-fold, without altering the equilibrium constant.

In contrast to the results of Inesi and co-workers, we were unable to simulate observed shifts in the calcium dependence of Ca-ATPase activity toward higher calcium concentrations associated with PLB inhibition without changing the equilibrium constant of step b. The PLB-induced reduction in K_b is consistent with the diminished cooperativity as calculated from the modified Hill equation (see eq 2) where a significant reduction in ΔG_b is observed (Table 1). Furthermore, our conclusion that PLB functions to selectively diminish the equilibrium constant associated with calcium activation is consistent with other models. Specifically, these results support earlier kinetic measurements of Mahaney and Froehlich that suggest that PLB stabilizes the E2 or apoform of the Ca-ATPase prior to calcium binding, such that under steady-state conditions the calcium-dependent activation of the Ca-ATPase is inhibited (*43*, *44*). Further, these results are consistent with recent mutagenesis and structural data that indicate that following association with the first calcium ion the structural rearrangements associated with calcium activation are necessary for the formation of the second high-affinity calcium binding site (*45*).

In conclusion, direct binding interactions between PLB and the Ca-ATPase nucleotide binding domain increases the activation barrier for the large amplitude structural changes associated with calcium activation and the formation of the second high-affinity calcium binding site whose occupancy is associated with enzyme activation (*5*, *46*). Since this inhibitory interaction requires PLB to assume an extended structure, the stabilization of the hinge region of PLB reduces the probability of the inhibitory association between the cytosolic domain of PLB and the nucleotide binding domain. Thus, phosphorylation of Ser^{16} and the concomitant stabilization of the interdomain linker in PLB function to release the inhibitory interaction between PLB and the Ca-ATPase to facilitate large-scale structural reorientations associated with calcium activation and nucleotide utilization.

REFERENCES

1. MacLennan, D. H., and Kranias, E. G. (2003) Phospholamban: a crucial regulator of cardiac contractility, *Nat. Rev. 4*, 566−577.
2. Toyoshima, C., and Inesi, G. (2004) Structural basis of ion pumping by Ca2+-ATPase of the sarcoplasmic reticulum, *Annu. Rev. Biochem. 73*, 269−292.
3. Berridge, M. J., Bootman, M. D., and Roderick, H. L. (2003) Calcium signalling: dynamics, homeostasis and remodeling, *Nat. Rev. Mol. Cell Biol. 4*, 517−529.
4. Cantilina, T., Sagara, Y., Inesi, G., and Jones, L. R. (1993) Comparative studies of cardiac and skeletal sarcoplasmic reticulum ATPases. Effect of a phospholamban antibody on enzyme activation by Ca^{2+}. *J. Biol. Chem. 268*, 17018−17025.
5. Inesi, G. (1987) Sequential mechanism of calcium binding and translocation in sarcoplasmic reticulum adenosine triphosphatase, *J. Biol. Chem. 262*, 16338−16342.
6. Zhang, Z., Lewis, D., Strock, C., Inesi, G., Nakasako, M., Nomura, H., and Toyoshima, C. (2000) Detailed characterization of the cooperative mechanism of Ca^{2+} binding and catalytic activation in the Ca^{2+} transport (SERCA) ATPase, *Biochemistry 39*, 8758−8767.
7. Inesi, G., Zhang, Z., and Lewis, D. (2002) Cooperative setting for long-range linkage of Ca^{2+} binding and ATP synthesis in the Ca^{2+}-ATPase, *Biophys. J. 83*, 2327−2332.
8. Toyoshima, C., and Nomura, H. (2002) Structural changes in the calcium pump accompanying the dissociation of calcium, *Nature 418*, 605−611.
9. Pollesello, P., Annila, A., and Ovaska, M. (1999) Structure of the 1−36 amino-terminal fragment of human phospholamban by nuclear magnetic resonance and modeling of the phospholamban pentamer, *Biophys. J.* 76, 1784−1795.
10. Pollesello, P., and Annila, A. (2002) Structure of the 1−36 N-terminal fragment of human phospholamban phosphorylated at Ser-16 and Thr-17, *Biophys. J. 83*, 484−490.
11. Lamberth, S., Schmid, H., Muenchbach, M., Vorherr, T., Krebs, J., Carafoli, E., and Griesinger, C. (2000) NMR structure of phospholamban, *Helv. Chim. Acta 83*, 2141−2152.
12. Zamoon, J., Mascioni, A., Thomas, D. D., and Veglia, G. (2003) NMR solution structure and topological orientation of monomeric phospholamban indodecylphosphocholine micelles, *Biophys. J. 85*, 2589−2598.
13. Metcalfe, E. E., Zamoon, J., Thomas, D. D., and Veglia, G. (2004) (1)H/(15)N heteronuclear NMR spectroscopy shows four dynamic domains for phospholamban reconstituted in dodecylphosphocholine micelles, *Biophys. J. 87*, 1205−1214.
14. Yao, Q., and Bigelow, D. J. (1998) Affinity purification of the Ca-ATPase from cardiac sarcoplasmic reticulum membranes, *Protein Expression Purif. 11*, 12−16.
15. Yao, Q., Bevan, J. L., Weaver, R. F., and Bigelow, D. J. (1996) Purification of porcine phospholamban expressed in *Escherichia coli*, *Protein Expression Purif. 8*, 463−468.
16. Li, J., Bigelow, D. J., and Squier, T. C. (2003) Phosphorylation by cAMP-dependent protein kinase modulates the structural coupling between the transmembrane and cytosolic domains of phospholamban, *Biochemistry 42*, 10674−10682.
17. Karim, C. B., Marquardt, C. G., Stamm, J. D., Barany, G., and Thomas, D. D. (2000) Synthetic null-cysteine phospholamban analogue and the corresponding transmembrane domain inhibit the Ca-ATPase, *Biochemistry 39*, 10892−10897.
18. Negash, S., Yao, Q., Sun, H., Li, J., Bigelow, D. J., and Squier, T. C. (2000) Phospholamban remains associated with the Ca^{2+}- and Mg^{2+}-dependent ATPase following phosphorylation by cyclic AMP-dependent protein kinase, *Biochem. J. 351*, 195−205.
19. Schaffner, W., and Weissmann, C. (1973) A rapid, sensitive, and specific method for the determination of protein in dilute solution, *Anal. Biochem. 56*, 502−514.
20. Lanzetta, P. A., Alvarez, L. J., Reinach, P. S., and Candia, D. A. (1979) An improved assay for nanomole amounts of inorganic phosphate, *Anal. Biochem. 100*, 95−97.
21. Fabiato, A. (1988) Computer programs for calculating total from specified free or free from specified total ionic concentrations in aqueous solutions containing multiple metals and ligands, *Methods Enzymol. 57*, 378−417.
22. Pedigo, S., and Shea, M. A. (1995) Discontinuous equilibrium titrations of cooperative calcium binding to calmodulin monitored by 1-D 1H-nuclear magnetic resonance spectroscopy, *Biochemistry 34*, 10676−10689.
23. Sreerama, N., and Woody, R. W. (2000) Estimation of protein secondary structure from circular dichroism spectra: comparison of CONTIN, SELCON, and CDSSTR methods with an expanded reference set, *Anal. Biochem. 287*, 252−260.
24. Chen, B., and Bigelow, D. J. (2002) Conformational transitions of phospholamban near the lipid-water interface, *Biochemistry 41*, 13965−13972.
25. Hunter, G. W., and Squier, T. C. (1998) Phospholipid acyl chain rotational dynamics are independent of headgroup structure in unilamellar vesicles containing binary mixtures of dioleoylphosphatidylcholine and dioleoyl-phosphatidylethanolamine, *Biochim. Biophys. Acta 1415*, 63−76.

26. Yao, Y., Schoneich, C., and Squier, T. C. (1994) Resolution of structural changes associated with calcium activation of calmodulin using frequency domain fluorescence spectroscopy, *Biochemistry 33*, 7797−7810.
27. Johnson, M. L., and Faunt, L. M. (1992) Parameter estimation by least-squares methods, *Methods Enzymol. 210*, 1−37.
28. Bevington, P. R. (1969) *Data Reduction and Error Analysis for the Physical Sciences*, McGraw-Hill, New York.
29. Lakowicz, J. R., and Gryczynski, I. (1991) Frequency-Domain Fluorescence Spectroscopy, in *Topics in Fluorescence Spectroscopy (*Lakowicz, J. R., Ed.) Vol. I, pp293−335, Plenum Press, New York.
30. Richardson, J. S, and Richardson, D. C. (1989) Principles and Patterns of Protein Conformation, in *Prediction of Protein Structure and the Principles of Protein Conformation* (Fasman, G. D., Ed.) pp 1−98, Plenum Press, New York.
31. Ferrington, D. A., Yao, Q., Squier, T. C., and Bigelow, D. J. (2002) Comparable levels of Ca-ATPase inhibition by phospholamban in slow-twitch skeletal and cardiac sarcoplasmic reticulum, *Biochemistry 41*, 13280−13296.
32. Li, J., Xiong, Y., Bigelow, D. J., and Squier, T. C. (2004) Phospholamban binds in a compact and ordered conformation to the Ca-ATPase, *Biochemistry 43*, 455−463.
33. Li, J., Bigelow, D. J., and Squier, T. C. (2004) Conformational changes within the cytosolic domain of phospholamban upon release of Ca-ATPase inhibition, *Biochemistry 43*, 3870−3879.
34. Mayer, E. J., McKenna, E., Garsky, V. M., Burke, C. J., Mach, H., Middaugh, C. R., Sardana, M., Smith, J. S., and Johnson, R. G., Jr. (1996) Biochemical and biophysical comparison of native and chemically synthesized phospholamban and a monomeric phospholamban analog, *J. Biol. Chem. 271*, 1669−1677.
35. James, P., Inui, M., Tada, M., Chiesi, M., and Carafoli, E. (1989) Nature and site of phospholamban regulation of the Ca2+ pump of sarcoplasmic reticulum, *Nature 342*, 90−92.
36. Toyofuku, T., Kurzydlowski, K., Tada, M., and MacLennan, D. H. (1994) Amino acids Lys-Asp-Asp-Lys-Pro-Val402 in the Ca(2+)-ATPase of cardiac sarcoplasmic reticulum are critical for functional association with phospholamban, *J. Biol. Chem. 269*, 22929−22932.
37. Jones, L. R., Cornea, R. L, and Chen, Z. (2002) Close proximity between residue 30 of phospholamban and cysteine 318 of the cardiac Ca2+ pump revealed by intermolecular thiol cross-linking, *J. Biol. Chem. 277*, 28319−28329.
38. Toyofuku, T., Kurzydlowski, K., Tada, M., and MacLennan, D. H. (1993) Identification of regions in the Ca(2+)-ATPase of sarcoplasmic reticulum that affect functional association with phospholamban, *J. Biol. Chem. 268*, 2809−2815.
39. Toyoshima, C., Asahi, M., Sugita, Y., Khanna, R., Tsuda, T., and MacLennan, D. H. (2003) Modeling of the inhibitory interaction of phospholamban with the Ca2+ ATPase, *Proc. Natl. Acad. Sci. U.S.A. 100*, 467−472.
40. Hutter, M. C., Krebs, J., Meiler, J., Griesinger, C., Carafoli, E., and Helms, V. (2002) A structural model of the complex formed by phospholamban and the calcium pump of sarcoplasmic reticulum obtained by molecular mechanics, *ChemBioChem 3* 1200−1208.
41. Tatulian, S. A., Chen, B., Li, J., Negash, S., Middaugh, C. R., Bigelow, D. J., and Squier, T. C. (2002) The inhibitory action of phospholamban involves stabilization of I-helices within the Ca-ATPase, *Biochemistry 41*, 741−751.
42. Negash, S., Huang, S., and Squier, T. C. (1999) Rearrangement of domain elements of the Ca-ATPase in cardiac sarcoplasmic reticulum membranes upon phospholamban phosphorylation, *Biochemistry 38*, 8150 − 8158.
43. Mahaney, J. E., Albers, R. W., Waggoner, J. R., Kutchai, H. C., and Froehlich, J. P. (2005) Intermolecular conformational coupling and free energy exchange enhance the catalytic efficiency of cardiac muscle SERCA2a following the relief of phospholamban inhibition, *Biochemistry 44*, 7713−7724.
44. Mahaney, J. E., Autry, J. M., and Jones, L. R. (2000) Kinetics studies of the cardiac Ca-ATPase expressed in Sf21 cells: new insights on Ca-ATPase regulation by phospholamban, *Biophys. J. 78*, 1306−1323.
45. Toyoshima, C., and Inesi, G. (2004) Structural basis of ion pumping by Ca2+-ATPase of the sarcoplasmic reticulum, *Annu. Rev. Biochem. 73*, 269−292.
46. Bigelow, D. J., and Squier, T. C. (2005) Redox modulation of cellular signaling and metabolism through reversible oxidation of methionines in calcium regulatory proteins, *Biochim. Biophys. Acta. 1703*, 121−134.
47. Guex, N., and Peitsch, M. C. (1997) SWISS-MODEL and the Swiss PdbViewer: an environment for comparative protein modeling, *Electrophoresis 18*, 2714−2723.
48. Zamoon, J., Mascioni, A., Thomas, D. D., and Veglia, G. (2003) NMR solution structure and topological orientation of monomeric phospholamban in dodecylphosphocholine micelles, *Biophys. J. 85*, 2589−2598.
49. Tsodikov, O. V., Record, M. T., and Sergeev, Y. V. (2002) A novel computer program for fast calculation of accessible and molecular surface areas and average surface curvature, *J. Comput. Chem. 23*, 600−609.
50. Beechem, J. M., Gratton, E., Ameloot, M., Knutson, J. R., and Brand, L. (1991) The Global Analysis of Fluorescence Intensity and Anisotropy Decay Data: Second-Generation Theory and Programs, in *Topics in Fluorescence Spectroscopy* (Lakowicz, J. R., Ed.) Vol. 2, pp 241−306, Plenum Press, New York.

BI051075O